Influence of Losses, Device Size, and Mode Confinement on Integrated Micro-Ring Resonator Performance for Absorption Spectroscopy Using Evanescent Field Sensing

P. Girault, L. Oyhenart, T. Rouanet, S. Joly, G. Beaudin, Michael Canva, L. Bechou, Paul Charette

Influence of losses, device size, and mode confinement on integrated micro-ring resonator performance for absorption spectroscopy using evanescent field sensing

P. Girault[1,2], L. Oyhenart[3], T. Rouanet[1,2,3], S. Joly[3], G. Beaudin[1,2], M. Canva[1,2], L. Bechou[1,2,3], and P.G. Charette[1,2]

[1]Laboratoire Nanotechnologies Nanosystèmes (LN2)-CNRS IRL-3463, Université de Sherbrooke, Sherbrooke, Québec, J1K 0A5, Canada
[2]Institut interdisciplinaire d'innovation technologique (3IT), Université de Sherbrooke, Sherbrooke, Québec, J1K 0A5, Canada
[3]Laboratoire de l'Intégration du Matériau au Système (IMS), University of Bordeaux, UMR CNRS 5218, Bordeaux INP, 351 Cours de la Libération, 33405 Talence, France

***Abstract*—This work presents a detailed modeling-based analysis of integrated micro-ring resonators used for absorption spectroscopy. Generally, sensors based on micro-ring resonators detect changes in the real part of the sensing medium refractive index, at critical coupling. In absorption spectroscopy, however, micro-ring resonators are used to measure changes in the imaginary part of the index and are most sensitive away from critical coupling, with separate maxima in the under- and over-coupled regimes. In this work, we present a detailed analysis of the under-coupled regime, explaining the relationships between sensitivity, mode confinement, and losses. The analysis is based on reverse-symmetry waveguides to increase the proportion of mode power in the sensing medium and incorporates a realistic model of propagation losses based on experimental measurements of sidewall roughness. The analysis demonstrates that the resonant nature of the sensor is most effective at small radii compared to a non-resonant structure of equal size and shows a behavior of diminishing returns at larger device sizes regarding sensitivity and elevated proportions of mode power in the evanescent field.**

***Index Terms*—Absorption spectroscopy, Biosensor, Integrated photonics, Optical resonators, Waveguides, Simulations**

I. Introduction

Fields such as environmental monitoring and agriculture have a growing need for sensitive, selective, and portable sensors for real-time monitoring of water quality [1]. Though conventional spectroscopic detection systems provide high-precision measurements, they remain costly and are generally not field-deployable [2]. Miniaturized sensors based on integrated photonics devices, such as micro-ring resonators (MRRs), have demonstrated high sensitivity at small dimensions suitable for miniaturized portable instruments [3]–[5].

MRRs rely on the interaction between the evanescent field from a guided mode in a ring resonator and a target species in the fluid in contact with the ring for detection. Most instances of biomolecular sensing with MRRs are based on surface affinity assays [6]–[9]. Though such surface-bound sensing has been successful in many applications, the surface functionalization chemistry remains one of the most complex, challenging, and costly aspects of integrated photonics sensor systems. Furthermore, there are many molecular targets for which no appropriate capture probe surface functionalization is available. To mitigate this problem, MRRs can instead rely on volume sensing. For example, a target-specific colorimetric reaction can induce a change in the bulk refractive index of the fluid and thus perturb the guided mode, eliciting a sensor response. Such volume-based sensing involves simpler chemistry and is not subject to surface saturation effects.

With integrated photonics devices, sensor response is generally believed to be optimal when the interaction between the sensing volume and the guided mode is maximized. Numerous waveguide structures have been studied for this purpose: slot [10], pedestal [11], substrate over-etch [12], sub-wavelength gratings [10]–[13], suspended [14], or "ultra-thin" [15], with varying degrees of fabrication complexity. Wavelength or/and intensity interrogation can be used [6], [16] and several studies propose guidelines for optimal geometric and material parameters in MRR-based sensing [6], [17], [18].

For conventional strip waveguides, a simple solution in principle to increase the interaction between the sensing volume and the guided mode is the use of reverse-symmetry waveguides [19], where the refractive index of the substrate (waveguide "bottom cladding") is lower than that of the fluid sensing medium ("top cladding"). However, it can be difficult in practice to find a solid material with the required mechanical properties having a refractive index lower than that of a fluid.

In most instances of MRR-based sensing, the presence of the target analyte mainly perturbs the real part of the refractive index in the sensing volume, causing a spectral shift in the ring resonance response. In contrast, the presence of the analyte may also elicit a change in the imaginary part of the refractive index (extinction coefficient). When changes in the imaginary

part of the refractive index are the main sensing event, this is often referred to as "absorption spectroscopy". While different optical devices such as fiber-based Bragg and long-period gratings [2], [20] or long range surface plasmon resonance [21] have been studied for absorption spectroscopy, relatively few studies have addressed the use of MRRs for this purpose [22]–[26].

With an MRR-based system (Fig. 1a), a perturbation in the extinction coefficient primarily causes a change in the depth of the response at resonance (Fig. 1c). This type of sensing could be used to detect a wide variety of pollutants in water, for example, with a colorimetric reaction that involves the complexation between a ligand and a target heavy metal ion where the resulting complex changes the absorption coefficient of the fluid medium [27], [28].

In previous work [29], we proposed an analytical approach to determine the maximum sensitivity of MRRs used for absorption spectroscopy. In particular, we showed that sensitivity as a function of the ring self-coupling coefficient exhibits two maxima, of equal magnitude and opposite sign, corresponding to over and under-coupled conditions occurring at distinct ring/bus gap sizes. The under-coupled sensitivity maximum corresponds to the larger of the two gap sizes, which is advantageous from a fabrication point of view (relaxed constraints for lithography).

In this paper, we continue this work to fully characterize the under-coupled regime. The analysis is based on a MRR model system with reverse-symmetry waveguides, leading to a greater range of interaction with the sensing volume and a more revealing analysis of the underlying phenomena. The relationship between propagation losses and waveguide core geometry is modeled using experimental data from SEM images. The analysis demonstrates that the MRR greatly improves the trade-off between sensitivity and size compared to a non-resonant structure, such as a spiral, which is advantageous for miniaturization (smaller footprint at equal sensitivity).

II. Analytical Model

A. Micro-ring resonator model system

The MRR model system is based on reverse-symmetry waveguides with a PMMA, poly(methyl methacrylate), core of refractive index n_{core} = 1.49, with width w and height h (Fig. 1b) [30]. The bulk fluid in the sensing medium is water (n_{water} = 1.33) and the substrate is porous silica (n_{sub} = 1.2) [31]. The MRR is defined by the ring radius R and gap g between the ring and bus waveguides (Fig. 1a). In many sensing applications, low cost fabrication is a desirable feature: as such, the model system is based on polymer core waveguides and geometry compatible with photolithography, though the analysis is valid for any material system and geometry. The analysis pertains to the fundamental TE mode as results for the TM mode are similar. The sensor response is the change in depth, or "contrast", of the optical transmission power spectrum at resonance through the bus waveguide.

As an example application, the study focuses on the detection of hexavalent chromium, Cr(VI), a pollutant in water. Cr(VI) is detected with diphenylcarbazide (DPC) by colorimetry, where the pair form a complex with an absorption peak

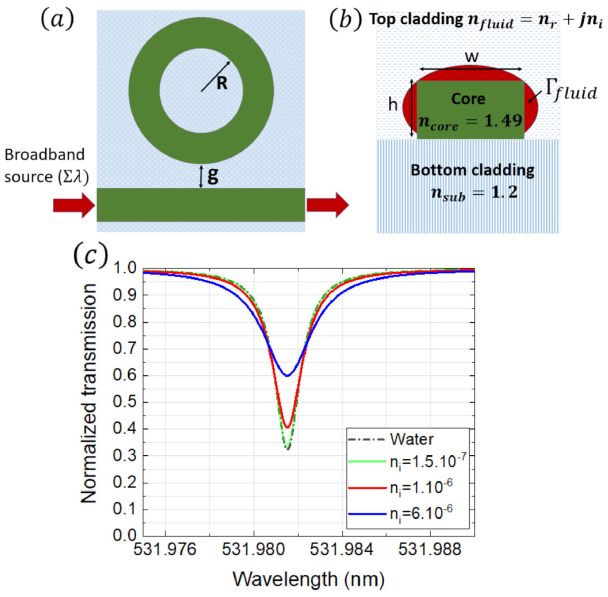

Fig. 1. (a) Micro-ring resonator (MRR) model system; (b) Cross-section of the reverse-symmetry waveguides; (c) Modeled transmission spectra (R = 50 μm, g = 460 nm, w = 0.7 μm, h = 0.28 μm, Γ_{fluid} = 26%) for discrete values of fluid medium extinction coefficients, n_i ($n_r = n_{water}$ = 1.33).

at 550 nm [28], [32], [33]. The resonance wavelength of the micro-ring resonator model system is 532 nm, a commonly available laser wavelength close to 550 nm. The refractive index of the sensing medium can be approximated as $n_{fluid} \approx n_r + jn_i$, where $n_r = n_{water}$. Fig. 1c shows the numerically modeled response of a MRR (R = 50 μm, g = 460 nm, w = 0.7 μm, h = 0.28 μm) for discrete values of n_i ranging from 1.5×10^{-7} to 6×10^{-6}, corresponding to concentrations of 10 μg/l to 1000 μg/l Cr(VI) in water.

B. Definition of sensitivity

In previous work [29], we showed that sensitivity for absorption spectroscopy with a MRR, defined as the ratio of change in transmitted optical power at the resonance wavelength through the bus waveguide, T, to change in the extinction coefficient of the fluid, n_i can be expressed as :

$$S = \frac{dT(n_i)}{dn_i} = \frac{4\pi}{\lambda_{res}} L\Gamma_{fluid} a \frac{(a-\tau)(1-\tau^2)}{(1-\tau a)^3} \qquad (1)$$

at resonance wavelength λ_{res}, ring length $L = 2\pi R$, round-trip amplitude transmission coefficient a, self-coupling coefficient τ, and fluid medium evanescent field ratio Γ_{fluid} (see below). In particular, we showed that maximum achievable sensitivity with respect to the bus-ring gap size in the under-coupled regime, S_{MRR}, can be expressed as:

$$S_{MRR} = \underbrace{\frac{4\pi}{\lambda_{res}} L\Gamma_{fluid} a^2}_{S_{NR}} \underbrace{\left| \frac{2}{3\sqrt{3}} \frac{1}{a(a^2-1)} \right|}_{S_e} \qquad (2)$$

where S_{NR} is the sensitivity of an equivalent non-resonant waveguide sensor (a straight waveguide, for example) of equal length and losses, while S_e is an enhancement factor due to the multiple revolutions in the ring.

C. Fluid medium evanescent field ratio

As indicated by (2), S_{MRR} is proportional to Γ_{fluid}, the "fluid medium evanescent field ratio", defined as the proportion of total mode power in the fluid sensing medium. Γ_{fluid} is calculated from the distribution of mode energy in the xy plane normal to the direction of propagation (Fig. 1b):

$$\Gamma_{fluid} = \frac{\int\int_{A_{fluid}} |E(x,y)|^2 \, dxdy}{\int\int_{\infty} |E(x,y)|^2 \, dxdy} \tag{3}$$

where A_{fluid} is the area occupied by the fluid and $E(x,y)$ is the electric field amplitude. Fig. 2 shows a map of Γ_{fluid} as a function of waveguide core dimensions that support single-mode operation for the fundamental TE mode at λ = 532 nm, where solutions to (3) were calculated numerically using a mode solver (FIMMWAVE, Photon Design). The analysis below is based on a fixed waveguide core width of 0.7 μm which is achievable with photolithography and yields a good selection of admissible core heights, corresponding to a range of fluid medium evanescent field ratios of approximately $25\% < \Gamma_{fluid} < 75\%$ (Fig. 2).

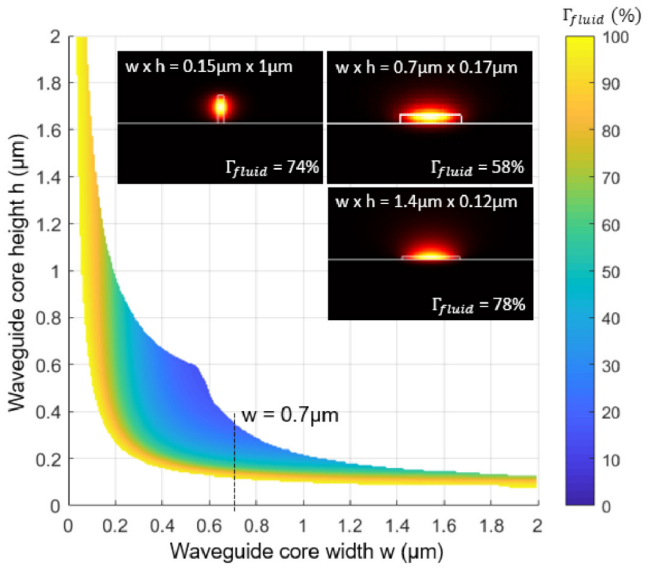

Fig. 2. Fluid medium evanescent field ratio, Γ_{fluid}, as a function of waveguide core dimensions that support single-mode operation at λ = 532 nm (TE mode). The inserts show modal E field intensity distributions for 3 examples of core dimensions, with corresponding values of Γ_{fluid}.

D. Round-trip transmission coefficient and loss components

The round-trip amplitude transmission coefficient in the ring, a, is defined as [34]:

$$a^2 = e^{-\alpha L} = e^{-(\alpha_{prop}+\alpha_{bend})L} \tag{4}$$

where α, the total mode power attenuation coefficient, is the sum of the waveguide propagation and bending loss coefficients, α_{prop} and α_{bend}.

In absorption spectroscopy, propagation losses can be approximated ($\tilde{\alpha}_{prop}$) by the sum of two components:

$$\alpha_{prop} \approx \tilde{\alpha}_{prop} = \Gamma_{fluid}\alpha_{fluid} + \alpha_{wg} \tag{5}$$

The first part of (5), $\Gamma_{fluid}\alpha_{fluid}$, represents the propagation losses due to absorption in the fluid sensing medium i.e., the physical parameter measured by the sensor. It is equal to the attenuation coefficient of the fluid, exemple de modification$\alpha_{fluid} = \frac{4\pi}{\lambda} n_i$, scaled by the proportion of total mode power in the fluid, Γ_{fluid}. In the analysis below, α_{fluid} = 0.23 cm^{-1} (1 dB/cm) for $n_i = 10^{-6}$ at λ = 532 nm, which corresponds to a 100 μg/L concentration of Cr(VI)-DPC in water [28].

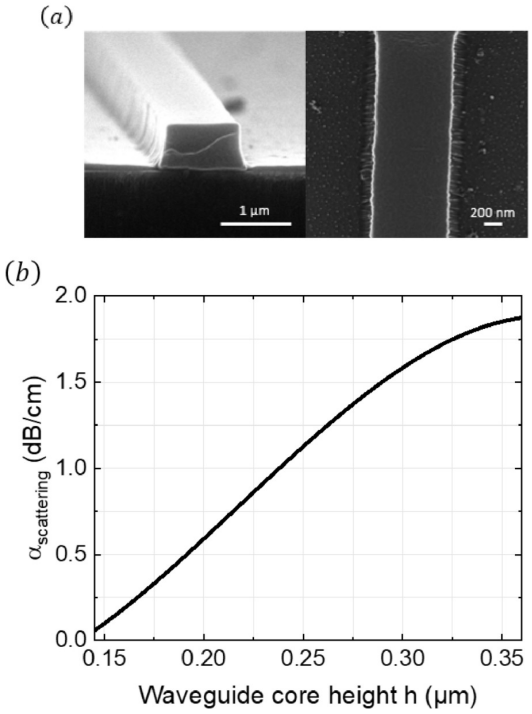

Fig. 3. (a) SEM cross-sectional and top view images of a PMMA strip waveguide on porous silica fabricated in our cleanrooms; (b) Modeled scattering losses from vertical sidewall roughness as a function of waveguide core height for a fixed waveguide core width of 0.7 μm.

The second part of (5), α_{wg}, represents the baseline propagation losses for the case of a near-lossless fluid medium (ex: water). Material losses in integrated photonics are generally very low and scattering from vertical sidewall roughness is typically the main source of propagation losses, where α_{wg} can be modeled by a function of core height, $\alpha_{wg} \approx \alpha_{scattering}(h)$, according to the well-known method by Payne and Lacey [35] adapted for 2D analysis. In this method, losses are related to the surface topology auto-correlation function, $R(u)$:

$$R(u) = \sigma^2 \exp\left(-\frac{|u|}{L_{cor}}\right) \tag{6}$$

where the auto-correlation length, L_{cor}, and the standard deviation, σ, can be estimated from atomic force microscopy (AFM) or scanning electron microscopy (SEM) images using

line edge roughness (LER) analysis [36], [37]. Application of LER analysis to SEM images of strip waveguides fabricated in our clean rooms (PMMA core on porous silica substrate, as shown for example in Fig. 3a) yielded the following estimates: L_{cor} = 50 $\pm$ 2 nm and σ = 6 nm. Fig. 3b shows the resulting modeled losses from sidewall roughness as a function of core height, $\alpha_{scattering}(h)$, for a core width of 0.7 μm.

III. Dependence of Sensitivity on Ring Radius and Proportion of Mode Power in the Fluid Medium

Fig. 4 shows plots of S_{MRR}, S_{NR}, and S_e in (2) as a function of ring radius for the case of Γ_{fluid} = 30% (waveguide core width = 0.7 μm, height = 0.26 μm). Interestingly, sensitivity reaches a maximum over a plateau bounded by radii values labeled R_e and R_{NR}, corresponding to the maxima of S_e and S_{NR}, respectively (see Appendix A for the derivation of analytical expressions for R_e and R_{NR})

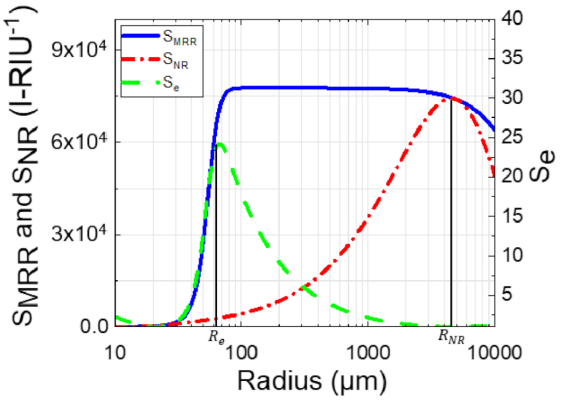

Fig. 4. MRR sensitivity, S_{MRR}, with components S_e and S_{NR}, as a function of ring radius for Γ_{fluid} = 30%. The radii R_e = 67 μm and R_{NR} = 4537 μm (maxima of S_e and S_{NR}) delimit the range over which the highest sensitivity is achieved. Waveguide core width = 0.7 μm, height = 0.26 μm.

Fig. 5 shows 2D maps of sensitivity, S_{MRR}, and round-trip losses in the ring, αL, as a function of waveguide core height or evanescent field ratio, versus ring radius (waveguide core width = 0.7 μm). The solid curves plot the (h, R) and (Γ_{fluid}, R) value pairs yielding the highest sensitivities and the dashed curves on either side indicate the values of R_e and R_{NR}. The data in the figure were generated using a custom open source Python program that calculates solutions to (2) based on a 2D polynomial model of $\tilde{\alpha}_{bend}(h, R)$ fitted to $\alpha_{bend}(h, R)$ data estimated numerically using a mode solver for a given value of w (see supplemental material). The highest sensitivities at each R (solid curves in Fig. 5a and 5b) were determined by non-linear minimization as a function of h.

The relative contributions of propagation and bending losses as a function of ring radius are at the root of the relationship between sensitivity and proportion of mode power in the fluid. To illustrate this in greater detail, Fig. 6 shows composite plots of 4 line profiles taken from Fig. 5b and Fig. 5c at select values of Γ_{fluid}: 20%, 45%, 65%, 75%. On the left vertical axis, the graphs show the total losses for a single round trip in the ring, αL, as a function of radius, as well as the individual loss contributions $\alpha_{prop}L$ and $\alpha_{bend}L$ (dashed lines). On the right

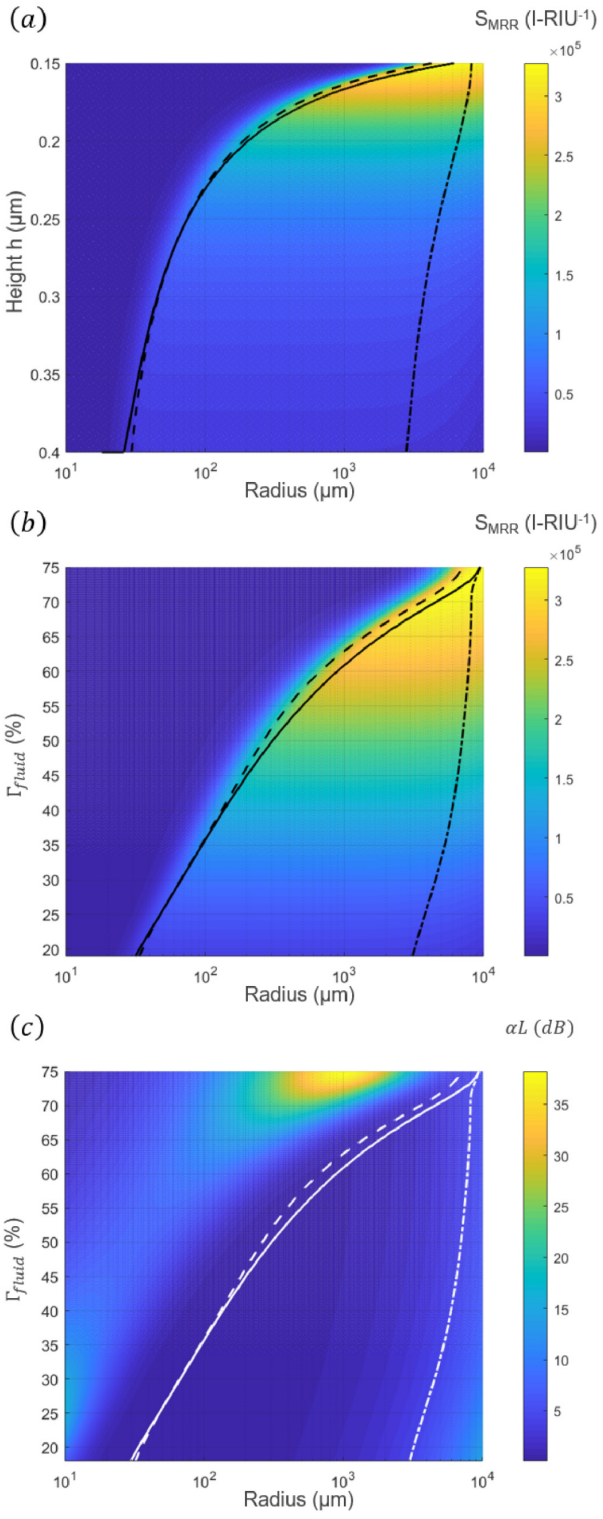

Fig. 5. (a) Sensitivity, S_{MRR}, as a function of waveguide core height versus ring radius; (b) Sensitivity and (c) round trip losses, αL, as a function of evanescent field ratio versus ring radius. The solid curves trace the value pairs for (h, R) in (a) and (Γ_{fluid}, R) in (b) and (c) yielding the highest sensitivities. The dashed curves on either side indicate values of R_e (left) and R_{NR} (right) as a function of h and Γ_{fluid}. Waveguide core width = 0.7 μm.

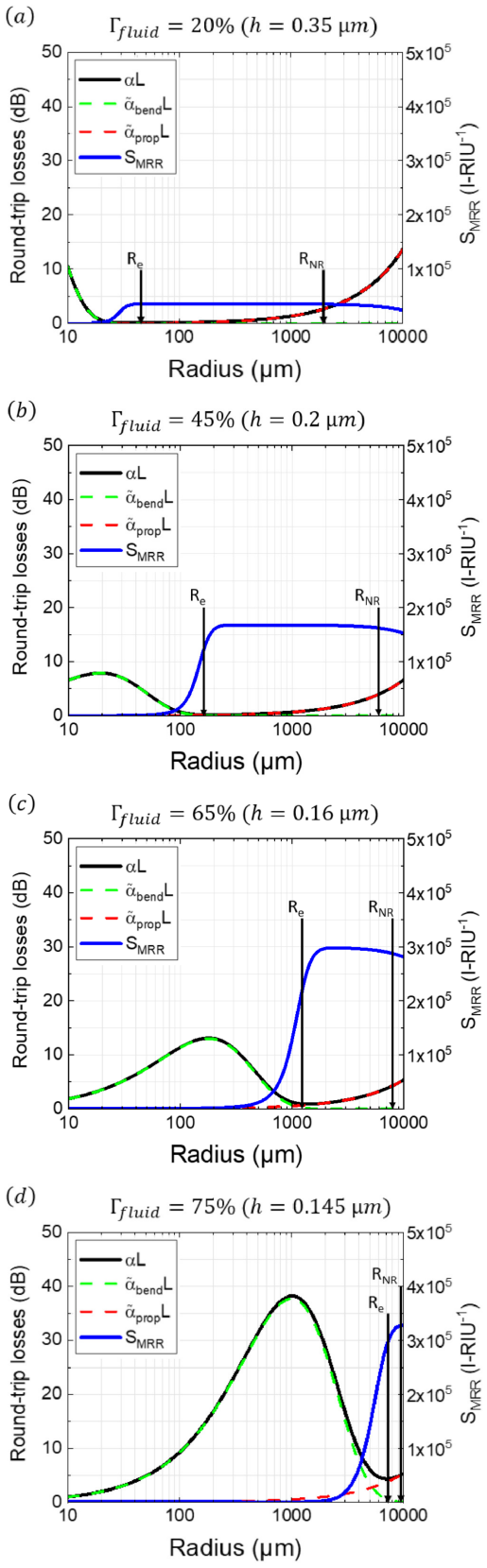

Fig. 6. Round-trip losses, $\alpha L = \tilde{\alpha}_{prop}L + \tilde{\alpha}_{bend}L$, and sensitivity as a function of radius for Γ_{fluid} = 20%, 45%, 65%, 75% (line profiles taken from Fig. 5b and Fig. 5c). Waveguide core width = 0.7 μm.

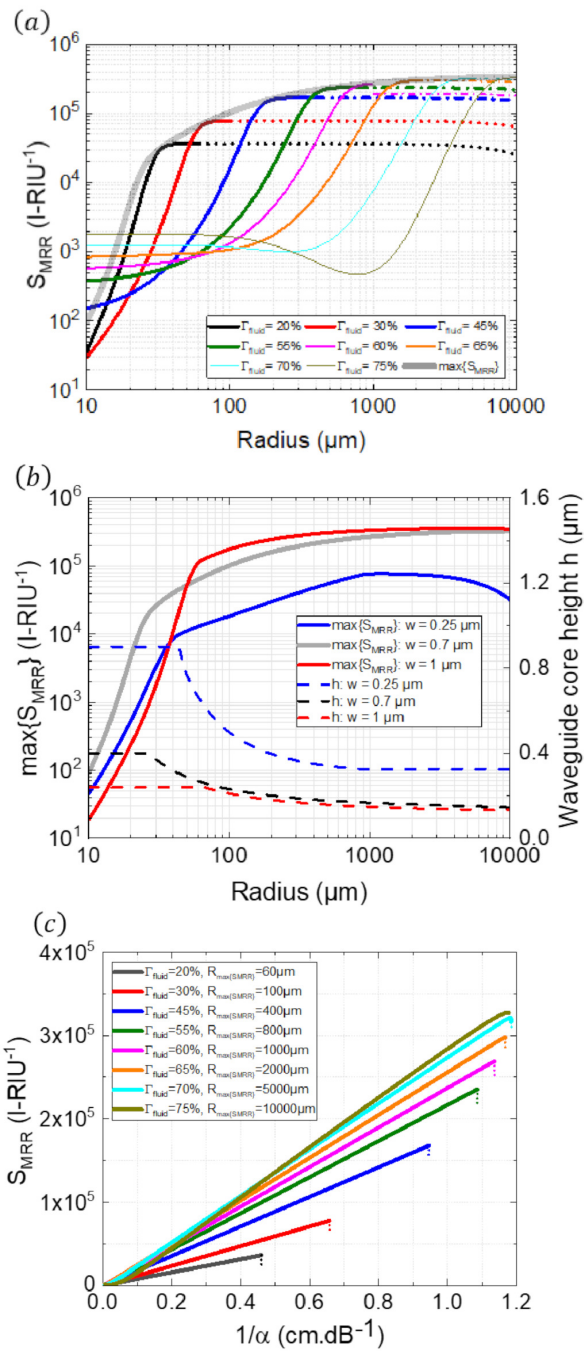

Fig. 7. (a) Sensitivity as a function of ring radius for select values of Γ_{fluid}, maximum achievable sensitivity as a function of radius is shown by the thick gray curve (core width = 0.7 μm); (b) Maximum achievable sensitivity as a function of ring radius for 3 different core widths (0.25 μm, 0.7 μm, 1 μm) along with the corresponding waveguide core heights; (c) Sensitivity as a function of $1/\alpha$ for the values of Γ_{fluid} in (a), the legend shows the radii for the highest achievable sensitivities at each Γ_{fluid} which correspond to the onset of the plateaus in (a) (core width = 0.7 μm).

vertical axis, the graphs show the corresponding sensitivity as a function of radius. For small values of Γ_{fluid} ($< 50\%$), bending losses dominate at small radii whereas propagation losses dominate at large radii, and both loss regimes are well separated in radius (Fig. 6a and 6b). As the proportion of mode power in the fluid medium increases, so does maximum

sensitivity since S_{MRR} is proportional to Γ_{fluid} (2). The maximum sensitivity plateaus at each Γ_{fluid} extend over the $[R_e, R_{NR}]$ intervals between the two loss regimes, where total losses are at their lowest, since S_{MRR} is proportional to the round-trip amplitude transmission coefficient, a, and therefore inversely related to losses, see (4). Note that total losses reach a minimum value at R_e since a is maximized at $R = R_e$, see (11). As Γ_{fluid} increases, bending losses become significant at ever larger ring radii, reducing the width of the $[R_e, R_{NR}]$ intervals and maximum sensitivity plateaus (Fig. 6a - 6c).

The dependence of S_{MRR} on Γ_{fluid} is illustrated in greater detail in Fig. 7a, showing a composite plot of line profiles from Fig. 5b at select values of Γ_{fluid}. In each case, sensitivity increases with radius until propagation losses dominate over bending losses, at which point sensitivity reaches a plateau. The thick gray curve in Fig. 7a shows the maximum achievable sensitivity as a function of radius, max$\{S_{MRR}\}$, i.e. the envelope of the sensitivity curves for distinct values of Γ_{fluid}.

Fig. 7b shows max$\{S_{MRR}\}$ curves for 3 different waveguide core widths: 0.25 μm, 0.7 μm, and 1 μm. At smaller radii ($R < \sim$50 μm), core geometries with aspect ratios closest to unity (ex: width = 0.7 μm) have comparatively lower bending losses due to higher mode confinement, both horizontally and vertically, leading to reduced MRR footprints at equal levels of maximum achievable sensitivity. At larger radii ($R > \sim$50 μm), wider core geometries (0.7 μm and 1 μm) have lower propagation losses and hence higher sensitivity, due to higher mode confinement horizontally (reduced sidewall height).

Fig. 7b also shows the core heights (dashed curves) as a function of radius corresponding to the values of max$\{S_{MRR}\}$ for the 3 values of core widths shown in Fig. 7a. The plateaus at the leftmost end of the curves indicate the range of radii for which bending losses dominate. In this regime, the highest sensitivity is achieved by minimizing bending losses, i.e. at the maximum allowed waveguide core heights that support single mode operation, hence the plateaus. As the ring radius increases, bending losses drop and propagation losses start to dominate (rightmost end of plateaus). Beyond this point, the waveguide core height can be reduced to raise the proportion of mode power in the fluid medium and thereby reach the optimal compromise between mode confinement and losses to achieve maximum sensitivity, though improvements are more modest beyond this point.

Fig. 7c shows sensitivity as a function of $1/\alpha$ for the values of Γ_{fluid} shown in Fig. 7a. The legend shows the radii at which highest sensitivity is achieved for each Γ_{fluid}, corresponding to the onset of the plateaus in Fig. 7a.Hence, sensitivity is proportional to $1/\alpha$ up to the point where propagation losses dominate over bending losses, whereby sensitivity reaches a plateau (solid curves in Fig. 7a). At very large radii, since propagation losses are constant and independent of radius ($\alpha = \alpha_{prop}$, thus $1/\alpha$ = constant) while sensitivity eventually decreases, the curves show a vertical drop at the ends.

IV. Sensing: Complex Index of Refraction, Ring Resonance Characteristics, and Coupling Regime

The analysis so far has concentrated on changes in the imaginary component of the fluid medium refractive index. Though this is indeed the main sensing event in absorption spectroscopy, the real and complex components of the index are linked through the Kramers-Kronig relations. Hence, a change in the extinction coefficient will be accompanied by a change in the real part of the refractive index. In previous work [28], we measured the extinction coefficient of Cr(VI)-DPC in water at various concentrations as a function of wavelength with a spectrometer (Varian UV-Vis, Agilent) and calculated the corresponding real parts of the index using the Kramers-Kronig relations (changes in the real part were below the resolution of the spectrometer). Based on these data, Fig. 8 shows the dependence of the real and imaginary components of the refractive index on concentration, as a function of wavelength (the derivatives were evaluated at a concentration of 100 μg/L). As expected, the figure shows that the maximum rate of change for the imaginary component at the absorption peak corresponds to a zero crossing for the real component [38]. Therefore, if simultaneous measurements at a single wavelength of changes in both the real and imaginary components of the index with respect to concentration are of interest [26], a MMR having a resonance wavelength that is a compromise between the sensitivities to either component is required.

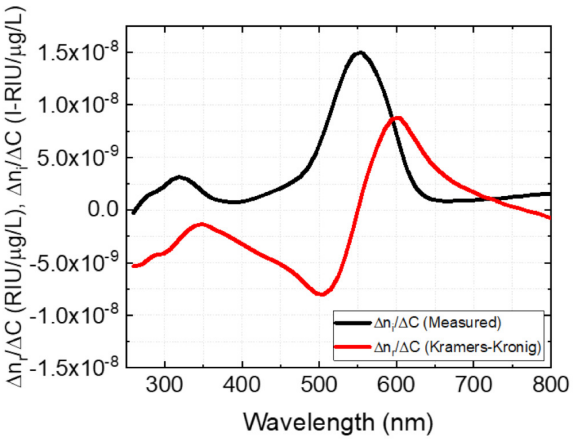

Fig. 8. Dependence of the imaginary ($\Delta n_i/\Delta C$, black curve) and real ($\Delta n_r/\Delta C$, red curve) components of the refractive index on concentration of Cr(VI)-DPC in water, as a function of wavelength. The curves are based on measurements of the imaginary part and calculations (Kramers-Kronig) of the corresponding real part of the refractive index.

Fig. 9 shows the ring Q factor (loaded) and the extinction ratio, ER (maximum transmission through the bus waveguide divided by the minimum at resonance, in dB), as a function of radius, for both the under-coupled and critically-coupled regimes. As expected, the under-coupled regime provides a higher Q factor, at the cost of a lower extinction ratio (the critically-coupled extinction ratio assumes a transmission minimum at resonance of 1%). Indeed, in certain demanding sensor applications, ring resonators are deliberately used in the

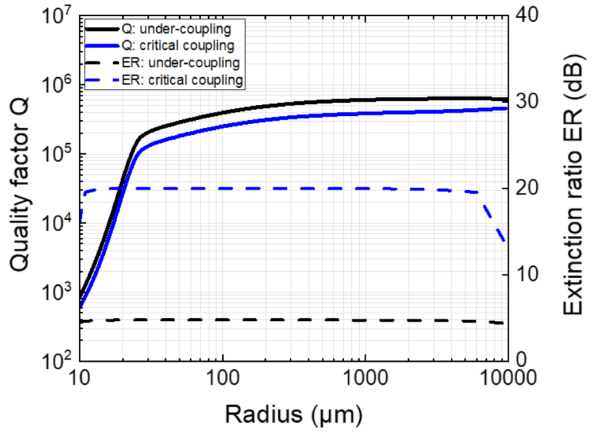

Fig. 9. Quality factor (Q) and extinction ratio (ER) as a function of ring radius for the critical coupling and under-coupling regimes (ER at critical coupling assumes a minimum transmission of 1%). Waveguide core width = 0.7 μm.

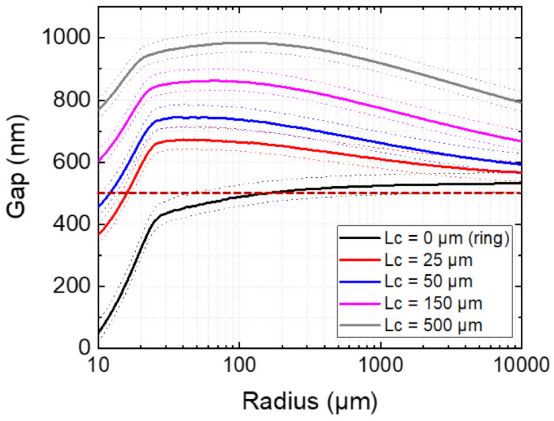

Fig. 10. Ring/bus gap size required for maximum MRR sensitivity as a function of radius. Black curve: circular ring; Other curves: racetracks with different straight sections of length L_c = 25 μm, 50 μm, 150 μm and 500 μm. The hashed lines above and below each solid curve indicate the fabrication tolerances for a $\pm 10\%$ variation in sensitivity. Waveguide core width = 0.7 μm.

under-couple regime to take advantage of the higher Q factor. In detection schemes based on peak shift tracking, the optimal ER for peak sharpness is 6 dB [17]. As seen in Fig. 9, the MRR model system has a near-optimal ER of ~5 dB.

V. Ring-bus gap size

In terms of fabricability, an important aspect of the MRR design is the size of the gap between the ring and bus waveguide. According to our previous work [29], MRR maximum sensitivity in the under-coupled regime (2) is reached at a ring self-coupling coefficient, τ, equal to:

$$\tau = \frac{\sqrt{3}a^2 - \sqrt{3} - 2a}{a^2 - 3} \tag{7}$$

For a given ring radius and waveguide core geometry, τ is set by the gap size. Hence, the gap size required for maximum MRR sensitivity is itself a function of the ring radius and the waveguide core geometry. The solid black curve in Fig. 10 shows the required ring/bus gap size as a function of radius for the MRR model system where the waveguide core has a constant width of 0.7 μm and an optimal core height given by Fig. 7b. Note that gap sizes are below the practical resolution limit for photolithography ($\sim$ 0.5 μm). If required, this can be remedied by adding short straight waveguide sections to the ring, parallel to the bus waveguide, to increase the length of the ring/bus coupling section (the ring resonator is considered a "racetrack"). This allows the gap to increase while maintaining maximum sensitivity. Fig. 10 gives examples of different length straight sections (25 μm, 50 μm, 150 μm and 500 μm) and their corresponding increasing optimal gap sizes. The hashed lines in Fig. 10 above and below the solid curves indicate the fabrication tolerances for a $\pm 10\%$ variation in sensitivity. Note also that for narrower waveguides (w < 0.5 μm), optimal gap sizes are above the photolithography resolution limit (data not shown).

VI. Comparison with non-resonant structure of equal square surface area: Archimedes Spiral

In order to objectively evaluate the absorption spectroscopy sensing performance of the MRR, its response is compared to two commonly used non-resonant structures: an Archimedes spiral [39]–[41] of equal outer radius (see Appendix B) and a simple straight waveguide of length equal to the diameter of the ring ($2R$). Fig. 11a shows plots of maximum achievable sensitivity as a function of ring radius for all three structures (here again, non-linear optimization is used to calculate maximum achievable sensitivity at each R with respect to waveguide core height). Three regimes can be roughly distinguished as a function of radius: a "small radius regime" (R < 200 μm) where the sensitivity for the MRR is the highest of the three sensor types at equal radii, a "medium radius regime" (200 μm < R < 5000 μm) where sensitivities of the MRR and the spiral are similar, and a "large radius regime" (R > 5000 μm) where a linear sensor (straight waveguide) performs as well as a 2D structure (MRR and spiral).

To give insight into this behavior, Fig. 11b show plots of the corresponding number of round-trips in the ring (N = Finesse/2π) and revolutions in the spiral. As seen in the figure, the MRR performs as a true ring resonator mainly in the "small radius regime", where the number of round trips in the ring is significant - note the high correlation with S_e (2). At very small radii, bending losses are high so that maximum sensitivity is achieved for relatively short interaction lengths, i.e. at low N. As the radius increases, bending losses drop and maximum sensitivity is achieved for higher N, peaking at $R \sim$ 30 μm. Afterwards, N decreases at the sensitivity maximum as propagation losses accumulate.

Intuitively, in the "small radius regime", the MRR could be considered as a spiral with overlapping rather than concentric rings, resulting in a higher sensitivity due to lower cumulative bending losses. At a radius of R = 50 μm for example, the MRR is over 10× more sensitive than the Archimedes

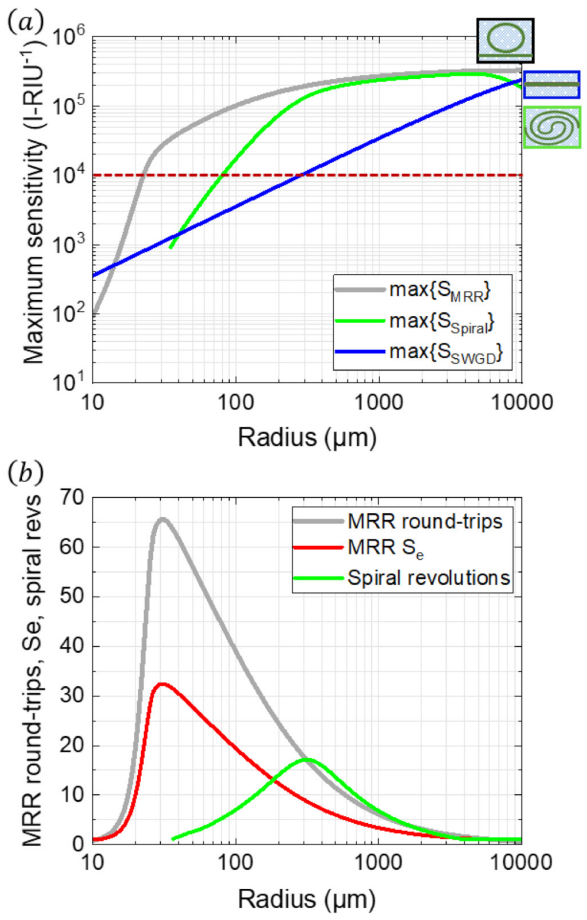

Fig. 11. (a) Maximum achievable sensitivity as a function of ring radius for the MRR (gray curve, as in Fig. 7b), spiral (green curve, outer spiral radius = MRR radius) and straight waveguide (SWGD, blue curve, length = 2× MRR radius). The pictograms at the top/right indicate the device type. The horizontal red dotted line indicates the minimum sensitivity required to resolve a 10^{-6} I-RIU change in the imaginary component of the fluid refractive index at an SNR of 20 dB; (b) Number of round-trips in the MRR (Finesse/2π, gray curve) and revolutions in the spiral (green curve) as a function of radius at maximum sensitivity. The red curve, S_e (2), is highly correlated with the the number of round-trips in the MRR. Waveguide core width = 0.7 μm.

spiral. In the "medium radius regime", light in the MRR and spiral undergoes a relatively small number of round-trips/revolutions in the structures though this still results in interaction distances with the sensing medium that are longer than for the straight waveguide, hence their higher sensitivities. Finally, in the "large radius regime", the number of round trips in the MRR and revolutions in the spiral are less than 1 for highest sensitivity, meaning that light only travels along a partial arc in both structures, closely approximating a straight waveguide.

In a physical system, measurement noise and sensitivity determine resolution, that is, the minimum resolvable signal level given a particular measurement signal-to-noise ratio. As an example, the red horizontal dotted line in Fig. 11a indicates the minimum sensitivity required to resolve a 10^{-6} I-RIU change in the imaginary component of the fluid refractive index at a signal-to-noise ratio of 20 dB. Under these conditions, a Archimedes spiral sensor requires a minimum radius of ~ 80 μm compared to a MRR which can be 5× smaller, a significant improvement for a miniaturized system.

VII. Conclusion

In this work, we presented a detailed modeling study of micro-ring resonators (MRR) in the under-coupled regime for absorption spectroscopy sensing. Compared to common strip waveguides, the reverse-symmetry waveguides in the model system enabled a much greater range of mode power fraction in the sensing medium to be considered. In addition, a realistic model of propagation losses based on experimental measurements of sidewall roughness was incorporated. The analysis showed that optimizing sensitivity for a particular set of requirements is not a simple matter of increasing the ring size and/or proportion of mode power in the sensing medium by reducing mode confinement. Indeed, the analysis showed a behavior of diminishing returns at larger device sizes regarding sensitivity and elevated levels of mode power in the evanescent field, where alternative structures that are simpler to fabricate may be more appropriate. This is contrary to the behavior of MRRs commonly used for sensing based on changes in the real part of the refractive index only, where increasing the ring radius generally yields a commensurate improvement in sensitivity compared to other devices of similar size. Indeed, a comparative analysis of sensing performance as a function of radius showed that the MRR is superior to a non-resonant structure of equal surface area (double Archimedes spiral) at small radii, where the number of round-trips in the ring at maximum sensitivity is significant. Though the MRR is potentially capable of simultaneously measuring changes in both the real and imaginary components of the fluid medium refractive index in response to changes in target analyte concentration, a ring having a resonance wavelength that is a compromise between the sensitivities to either component is required in this case. The analysis presented here can be applied to any MRR waveguide geometry and material system, as well as to MRR physical implementations other than integrated photonics such as optical fibers [42].

Acknowledgments

The authors gratefully acknowledge financial support for this work from the Agence Nationale de la Recherche (ANR) of France (Programme investissements d'avenir, Programme IdEx Bordeaux – LAPHIA, ANR-10-IDEX-03-02), the Natural Sciences and Engineering Research Council (NSERC) of Canada (Discovery Grants of Laurent Béchou, Paul Charette and Michael Canva), and the IRL-LN2. The LN2 is a CNRS International Research Laboratory (IRL) located at the Université de Sherbrooke, co-funded by the Université de Sherbrooke, the Centre National de la Recherche Scientifique (CNRS) of France, the École Centrale Lyon (ECL), the Institut National des Sciences Appliquées de Lyon (INSA Lyon), the Université Grenoble Alpes (UGA), and the Fonds de Recherche du Québec - Nature et Technologies (FRQNT).

APPENDIX A
ANALYTICAL MODELS OF R_e AND R_{NR}

R_e and R_{NR} are calculated by finding the extrema of S_e and S_{NR} with respect to R. Partial derivatives of a^2 and a with respect to R are required where, from (4) and (10):

$$\begin{aligned}\frac{\partial a^2}{\partial R} &= a^2 \frac{\partial}{\partial R}\left\{-(2\pi R)\left(\tilde{\alpha}_{prop}+\tilde{\alpha}_{bend}\right)\right\} \\ &= -2\pi a^2\left\{\frac{\partial}{\partial R}R\tilde{\alpha}_{prop}+\frac{\partial}{\partial R}R\tilde{\alpha}_{bend}\right\} \\ &= -2\pi a^2\left\{\tilde{\alpha}_{prop}+\tilde{\alpha}_{bend}-RB\tilde{\alpha}_{bend}\right\}\end{aligned}$$

thus:

$$\frac{\partial a^2}{\partial R} = -2\pi a^2\left\{\tilde{\alpha}_{prop}+(1-RB)\,\tilde{\alpha}_{bend}\right\} \tag{8}$$

and since:

$$\frac{\partial a^2}{\partial R} = 2a\frac{\partial a}{\partial R}$$

then:

$$\frac{\partial a}{\partial R} = \frac{1}{2a}\frac{\partial a^2}{\partial R} \tag{9}$$

Bending losses can be modeled ($\tilde{\alpha}_{bend}$) by an exponential function of the ring radius:

$$\tilde{\alpha}_{bend} = Ae^{-BR} \tag{10}$$

where parameters A and B depend on the excitation wavelength, ring geometry and materials, and can be fitted to mode loss data obtained numerically with a mode solver.

A. Analytical model of R_e

From (2):

$$S_e = \frac{2}{3\sqrt{3}}\frac{1}{a(a^2-1)}$$

Taking the partial derivative of S_e w/r to R to find the extrema:

$$\begin{aligned}\frac{\partial S_e}{\partial R} &= \frac{\partial}{\partial R}\left\{\frac{2}{3\sqrt{3}}\frac{1}{a(a^2-1)}\right\} \\ &= \frac{2}{3\sqrt{3}}\left\{\frac{-1}{a^2(a^2-1)}\frac{\partial a}{\partial R}+\frac{-1}{a(a^2-1)^2}\frac{\partial a^2}{\partial R}\right\}\end{aligned}$$

using (9) for $\partial a/\partial R$:

$$\begin{aligned}\frac{\partial S_e}{\partial R} &= \frac{2}{3\sqrt{3}}\left\{\frac{-1}{a^2(a^2-1)}\left(\frac{1}{2a}\frac{\partial a^2}{\partial R}\right)+\frac{-1}{a(a^2-1)^2}\frac{\partial a^2}{\partial R}\right\} \\ &= \frac{2}{3\sqrt{3}}\left\{\frac{-1}{2a^3(a^2-1)}\frac{(a^2-1)}{(a^2-1)}+\frac{-1}{a(a^2-1)^2}\frac{2a^2}{2a^2}\right\}\frac{\partial a^2}{\partial R} \\ &= \frac{2}{3\sqrt{3}}\left\{\frac{-a^2+1}{2a^3(a^2-1)}+\frac{-2a^2}{2a^3(a^2-1)^2}\right\}\frac{\partial a^2}{\partial R} \\ &= \frac{1}{3\sqrt{3}}\left\{\frac{(1-3a^2)}{2a^3(a^2-1)}\right\}\frac{\partial a^2}{\partial R}\end{aligned}$$

The extrema are found by solving:

$$\frac{\partial a^2}{\partial R} = 0 \tag{11}$$

and hence from (8) by solving:

$$\tilde{\alpha}_{prop}+(1-BR)\,\tilde{\alpha}_{bend} = 0$$

using (10):

$$(1-BR)\,e^{-BR} = \frac{1}{A}\tilde{\alpha}_{prop}$$

multiplying both sides by e:

$$(1-BR)\,e^{(1-BR)} = -\frac{e}{A}\tilde{\alpha}_{prop} \tag{12}$$

Equation (12) is of the form $ye^y = x$, where $y = (1-BR)$ and $x = -\frac{e}{A}\tilde{\alpha}_{prop}$. The equation can be solved using the Lambert function, $y = W_k(x)$, which has two solutions (k = 0,-1) for real values of x (the Lambert function must be calculated numerically, for example using a tool such as Matlab or Python). The solution for $k = 0$ is:

$$1-BR_e = W_0\left(-\frac{e}{A}\tilde{\alpha}_{prop}\right),\ \text{for}\ -\frac{e}{A}\tilde{\alpha}_{prop} \geq 0$$

thus:

$$R_e = \frac{1}{B}\left\{1-W_0\left(-\frac{e}{A}\tilde{\alpha}_{prop}\right)\right\},\ \text{for}\ \tilde{\alpha}_{prop} \leq 0 \tag{13}$$

The above solution is not of interest because losses cannot be negative. The correct solution is given by $k = -1$:

$$1-BR_e = W_{-1}\left(-\frac{e}{A}\tilde{\alpha}_{prop}\right),\ \text{for}\ \frac{-1}{e} \leq -\frac{e}{A}\tilde{\alpha}_{prop} < 0$$

thus:

$$R_e = \frac{1}{B}\left\{1-W_{-1}\left(-\frac{e}{A}\tilde{\alpha}_{prop}\right)\right\},\ \text{for}\ \tilde{\alpha}_{prop} \leq \frac{A}{e^2} \tag{14}$$

B. Analytical model of R_{NR}

From (2):

$$S_{NR} = \frac{4\pi}{\lambda_{res}}L\Gamma_{fluid}a^2 \tag{15}$$

Taking the partial derivative of S_{NR} with respect to R to find the extrema:

$$\begin{aligned}\frac{\partial S_{NR}}{\partial R} &= \frac{4\pi}{\lambda}\Gamma_{fluid}\left(\frac{\partial L}{\partial R}a^2+L\frac{\partial a^2}{\partial R}\right) = 0 \\ &= \frac{8\pi^2}{\lambda}\Gamma_{fluid}\,a^2\left(1+\frac{R}{a^2}\frac{\partial a^2}{\partial R}\right) = 0\end{aligned}$$

which can be solved with:

$$\left(1+\frac{R}{a^2}\frac{\partial a^2}{\partial R}\right) = 0$$

using (8) for $\partial a^2/\partial R$:

$$1+\frac{R}{a^2}\left(-2\pi a^2\left\{\tilde{\alpha}_{prop}+(1-BR)\,\tilde{\alpha}_{bend}\right\}\right) = 0$$

$$R\left\{\tilde{\alpha}_{prop} + (1 - BR)\,\tilde{\alpha}_{bend}\right\} = \frac{1}{2\pi} \tag{16}$$

The above equation must be solved for R_{NR} by non-linear minimization. However, for $\tilde{\alpha}_{bend} << \tilde{\alpha}_{prop}$, Equation (16) reduces to the solution for the optimal length of a straight waveguide used for absorption-based sensing, $L_{SWGD-opt}$ [41], [43], [44]:

$$R_{NR} \approx \frac{L_{SWGD-opt}}{2\pi} = \frac{1}{2\pi\tilde{\alpha}_{prop}}, \text{ for } \tilde{\alpha}_{bend} << \tilde{\alpha}_{prop} \tag{17}$$

APPENDIX B
ARCHIMEDES SPIRAL

The non-resonant structure used for comparison in the analysis is a "double" Archimedes spiral (see Fig. 12b). The double spiral is formed by two parallel waveguides of width w separated by a distance d. The outer (output) spiral is joined to the inner (input) spiral by an S-bend at the center. The Archimedes spiral is governed by the equation:

$$r(\theta) = a + b \times \theta \tag{18}$$

where r is the radius of the waveguide, θ is the angle between the x axis and the radius vector, $b/(2\pi)$ is the spacing between concentric spiral rings with $b/(2\pi) = 2 \times (w + d)$ for the double spiral, and a is the spiral offset from the origin at θ = 0. The MRR and spiral have the same square surface area for R (MRR radius) equal to the outer spiral radius.

The solid black line in Fig. 12a shows the maximum achievable sensitivity, $\max\{S_{Spiral}\}$, as a function of outer spiral radius. As with the MRR, $\max\{S_{Spiral}\}$ values at each r are obtained by non-linear optimization, in this case with respect to both waveguide core height (corresponding values are shown by the dashed line in the figure) and number of revolutions in the spiral (constrained to be ≥ 1, see Fig. 11b). Similarly to the MRR, bending losses in the spiral are high at smaller radii so maximum sensitivity is achieved at relatively short interaction lengths, i.e. at low numbers of revolutions in the spiral. As the radius increases, propagation losses start to dominate and maximum sensitivity is achieved at longer interaction lengths (higher numbers of revolutions). At $R \sim 300$ μm, the number of revolutions starts to decrease to maintain the optimum interaction length at increasing radii.

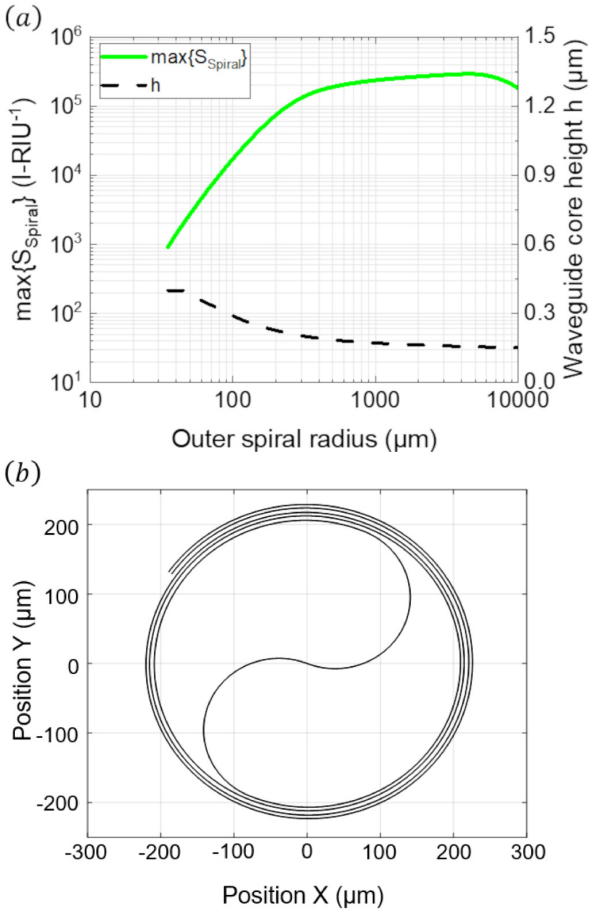

Fig. 12. (a) Maximum achievable sensitivity for a double Archimedes spiral as a function of outer spiral radius, with corresponding waveguide core height; (b) Diagram of a double Archimedes spiral. Waveguide core width = 0.7 μm, spacing between inner and outer waveguides = 5 μm.

REFERENCES

[1] Nevetha Yogarajah and Scott S. H. Tsai. Detection of trace arsenic in drinking water: challenges and opportunities for microfluidics. *Environ. Sci. Water Res. Technol.*, 4:426–447, 2015.

[2] Ya-nan Zhang, Yang Sun, Lu Cai, Yiping Gao, and Yi Cai. Optical fiber sensors for measurement of heavy metal ion concentration: A review. *Measurement*, 158:107742, 2020.

[3] Caterina Ciminelli, Clarissa Martina Campanella, Francesco Dell'Olio, Carlo Edoardo Campanella, and Mario Nicola Armenise. Label-free optical resonant sensors for biochemical applications. *Prog. Quantum. Electron.*, 37(2):51–107, 2013.

[4] Kevin D. Heylman, Kassandra A. Knapper, Erik H. Horak, Morgan T. Rea, Sudheer K. Vanga, and Randall H. Goldsmith. Optical microresonators for sensing and transduction: A materials perspective. *Adv. Mater.*, 29(30):1700037, 2017.

[5] Enxiao Luan, Hossam Shoman, Daniel Ratner, Karen Cheung, and Lukas Chrostowski. Silicon photonic biosensors using label-free detection. *Sensors*, 18(10):3519, 2018.

[6] Chung-Yen Chao and L. Jay Guo. Design and optimization of microring resonators in biochemical sensing applications. *J. Light. Technol.*, 24(3):1395–1402, 2006.

[7] David Chauvin, Jérémy Bell, Isabelle Leray, Isabelle Ledoux-Rak, and Chi Thanh Nguyen. Label-free optofluidic sensor based on polymeric microresonator for the detection of cadmium ions in tap water. *Sens. Actuators B Chem.*, 280:77–85, 2019.

[8] Jiawei Wang, Mariana Medina Sanchez, Yin Yin, Raffael Herzer, Libo Ma, and Oliver G. Schmidt. Silicon-based integrated label-free optofluidic biosensors: latest advances and roadmap. *Adv. Mater. Technol.*, 5(6):1901138, 2020.

[9] Zhongbo Zhang, Xufeng Zhang, Tijana Rajh, and Supratik Guha. Photonic microresonator based sensor for selective nitrate ion detection. *Sens. Actuators B Chem.*, 328:129027, 2021.

[10] Xu Wang, Jonas Flueckiger, Shon Schmidt, Samantha Grist, Sahba T. Fard, James Kirk, Matt Doerfler, Karen C. Cheung, Daniel M. Ratner, and Lukas Chrostowski. A silicon photonic biosensor using phase-shifted Bragg gratings in slot waveguide. *J. Biophotonics*, 6(10):821–828, 2013.

[11] Ching-Wen Chang, Xiaochuan Xu, Swapnajit Chakravarty, Hui-Chun Huang, Li-Wei Tu, Quark Yungsung Chen, Hamed Dalir, Michael A. Krainak, and Ray T. Chen. Pedestal subwavelength grating metamaterial waveguide ring resonator for ultra-sensitive label-free biosensing. *Biosens. Bioelectron.*, 141:111396, 2019.

[12] Enxiao Luan, Kashif M. Awan, Karen C. Cheung, and Lukas Chrostowski. High-performance sub-wavelength grating-based resonator sensors with substrate overetch. *Opt. Lett.*, 44(24):5981, 2019.

[13] Zhengsen Ruan, Nan Zhou, Shuang Zheng, Xiaoping Cao, Yun Long, Lin Chen, and Jian Wang. Releasing the light field in subwavelength grating slot microring resonators for athermal and sensing applications. *Nanoscale*, 12(29):15620–15630, 2020.

[14] Girija Gaur, Shuren Hu, Raymond L. Mernaugh, Ivan I. Kravchenko, Scott T. Retterer, and Sharon M. Weiss. Label-free detection of Herceptin® using suspended silicon microring resonators. *Sens. Actuators B Chem.*, 275:394–401, 2018.

[15] Sahba Talebi Fard, Valentina Donzella, Shon A. Schmidt, Jonas Flueckiger, Samantha M. Grist, Pouria Talebi Fard, Yichen Wu, Rick J. Bojko, Ezra Kwok, Nicolas A. F. Jaeger, Daniel M. Ratner, and Lukas Chrostowski. Performance of ultra-thin SOI-based resonators for sensing applications. *Opt. Express*, 22(12):14166, 2014.

[16] Zhengrui Tu, Dingshan Gao, Meiling Zhang, and Daming Zhang. High-sensitivity complex refractive index sensing based on Fano resonance in the subwavelength grating waveguide micro-ring resonator. *Opt. Express*, 25(17):20911, 2017.

[17] Misha Sumetsky. Optimization of optical ring resonator devices for sensing applications. *Opt. Lett.*, 32(17):2577, 2007.

[18] Ian M. White and Xudong Fan. On the performance quantification of resonant refractive index sensors. *Opt. Express*, 16(2):1020, 2008.

[19] Robert Horváth, Lars R. Lindvold, and Niels B. Larsen. Reverse-symmetry waveguides: theory and fabrication. *Appl. Phys. B: Lasers Opt*, 74(4-5):383–393, 2002.

[20] Xavier Daxhelet and Mykola Kulishov. Theory and practice of long-period gratings: when a loss becomes a gain. *Opt. Lett.*, 28(9):686–688, 2003.

[21] Vincent Chabot, Yannick Miron, Michel Grandbois, and Paul G. Charette. Long range surface plasmon resonance for increased sensitivity in living cell biosensing through greater probing depth. *Sens. Actuators B Chem.*, 174:94–101, 2012.

[22] Arthur Nitkowski, Long Chen, and Michal Lipson. Cavity-enhanced on-chip absorption spectroscopy using microring resonators. *Opt. Express*, 16(16):11930–11936, 2008.

[23] Todd H. Stievater, Marcel W. Pruessner, Doewon Park, William S. Rabinovich, R. Andrew McGill, Dmitry A. Kozak, Robert Furstenberg, Scott A. Holmstrom, and Jacob B. Khurgin. Trace gas absorption spectroscopy using functionalized microring resonators. *Opt. Lett.*, 39(4):969, 2014.

[24] Sheng Hu, Zhenming Hu, and Qiaoyun Wang. Determination of hexavalent chromium with a high-performance optical microring resonator. *Instrum Sci Technol.*, 45(6):593–604, 2017.

[25] Zhengrui Tu, Dingshan Gao, Meiling Zhang, and Daming Zhang. High-sensitivity complex refractive index sensing based on Fano resonance in the subwavelength grating waveguide micro-ring resonator. *Opt. Express*, 25(17):20911–20922, 2017.

[26] Raghi S. El Shamy, Mohamed A. Swillam, and Xun Li. On-chip complex refractive index detection at multiple wavelengths for selective sensing. *Sci. Rep.*, 12(1):9343, 2022.

[27] Ali Q. Alorabi, Mohamed Abdelbaset, and Sami Zabin. Colorimetric detection of multiple metal ions using schiff base 1-(2-thiophenylimino)-4-(n-dimethyl)benzene. *Chemosensors*, 8:1, 2020.

[28] Farida Meziane, Vincent Raimbault, Hamida Hallil, Simon Joly, Véronique Conédéra, Jean-Luc Lachaud, Laurent Béchou, Dominique Rebière, and Corinne Dejous. Study of a polymer optical microring resonator for hexavalent chromium sensing. *Sens. Actuators B Chem.*, 209:1049–1056, 2015.

[29] Miguel Diez Garcia, Pauline Girault, Simon Joly, Laurent Oyhenart, Vincent Raimbault, Corinne Dejous, and Laurent Bechou. An analytical approach to predict maximal sensitivity of microring resonators for absorption spectroscopy. *J. Light. Technol.*, 37(21):5500–5506, 2019.

[30] Dominique Bosc, Azar Maalouf, Frederic Henrio, and Séverine Haesaert. Strengthened poly(methacrylate) materials for optical waveguides and integrated functions. *Opt. Mater.*, 30(10):1514–1520, 2008.

[31] Pauline Girault, Nathalie Lorrain, Jonathan Lemaitre, Luiz Poffo, Mohamed Guendouz, Isabelle Hardy, Michel Gadonna, Aldo Gutierrez, Loïc Bodiou, and Joël Charrier. Racetrack micro-resonators based on ridge waveguides made of porous silica. *Opt. Mater.*, 50:167–174, 2015.

[32] Ronald T. Pflaum and Lester C. Howick. The chromium-diphenylcarbazide reaction. *J. Am. Chem. Soc.*, 78(19):4862–4866, 1956.

[33] Annija Lace, David Ryan, Mark Bowkett, and John Cleary. Chromium monitoring in water by colorimetry using optimised 1,5-diphenylcarbazide method. *Int. J. Environ. Res. Public Health*, 16(10):1803, 2019.

[34] Wim Bogaerts, Peter De Heyn, Thomas Van Vaerenbergh, Katrien De Vos, Shankar Kumar Selvaraja, Tom Claes, Pieter Dumon, Peter Bienstman, Dries Van Thourhout, and Roel Baets. Silicon microring resonators. *Laser Photonics Rev.*, 6(1):47–73, 2012.

[35] Frank P. Payne and Jonathan P. R. Lacey. A theoretical analysis of scattering loss from planar optical waveguides. *Opt. Quantum Electron.*, 26(10):977–986, 1994.

[36] George P. Patsis, Vassilios Constantoudis, Angeliki Tserepi, Evangelos Gogolides, and Grozdan Grozev. Quantification of line-edge roughness of photoresists. i. a comparison between off-line and on-line analysis of top-down scanning electron microscopy images. *J. Vac. Sci. Technol. B:Nanotechnol. Microelectron.*, 21(3):1008–1018, 2003.

[37] Maria Chiara Ubaldi, V. Stasi, Davide Piccinin, and Mario Martinelli. Molecular roughness analysis of developed resist by LER method. *Microelectron. Eng.*, 84(5-8):1088–1091, 2007.

[38] Thomas G. Mayerhöfer, Alicja Dabrowska, Andreas Schwaighofer, Bernhard Lendl, and Jürgen Popp. Beyond Beer's law: why the index of refraction depends (almost) linearly on concentration. *ChemPhysChem*, 21(8):707–711, April 2020.

[39] Wei Li, P. Anantha, Kwang Hong Lee, Hao Dong Qiu, Xin Guo, Simon Chun Kiat Goh, Lin Zhang, Hong Wang, Richard A. Soref, and Chuan Seng Tan. Spiral waveguides on germanium-on-silicon nitride platform for mid-IR sensing applications. *IEEE Photonics J.*, 10(3):1, 2018.

[40] Aldo Gutierrez-Arroyo, Emeline Baudet, Loïc Bodiou, Jonathan Lemaitre, Isabelle Hardy, François Faijan, Bruno Bureau, Virginie Nazabal, and Joël Charrier. Optical characterization at 7.7 μm of an integrated platform based on chalcogenide waveguides for sensing applications in the mid-infrared. *Opt. Express*, 24(20):23109–23117, 2016.

[41] Eva Ryckeboer, Ronny Bockstaele, Michael Vanslembrouck, and Roel Baets. Glucose sensing by waveguide-based absorption spectroscopy on a silicon chip. *Biomed. Opt. Express*, 5(5):1636, 2014.

[42] Vasileia Melissinaki, Odysseas Tsilipakos, Maria Kafesaki, Maria Farsari, and Stavros Pissadakis. Micro-Ring Resonator Devices Prototyped on Optical Fiber Tapers by Multi-Photon Lithography. *IEEE J. Sel. Top. Quantum Electron.*, 27(6):1–7, 2021.

[43] Aldo Gutierrez-Arroyo, Emeline Baudet, Loïc Bodiou, Virginie Nazabal, Emmanuel Rinnert, Karine Michel, Bruno Bureau, Florent Colas, and Joël Charrier. Theoretical study of an evanescent optical integrated sensor for multipurpose detection of gases and liquids in the Mid-Infrared. *Sens. Actuators B Chem.*, 242:842–848, 2017.

[44] Rami Zegadi, Nathalie Lorrain, Loïc Bodiou, Mohammed Guendouz, Lahcene Ziet, and Joël Charrier. Enhanced mid-infrared gas absorption spectroscopic detection using chalcogenide or porous germanium waveguides. *J. Opt.*, 23(3):035102, 2021.

P. Girault obtained her MSc in nanotechnologies at the Université de Nantes (France) in 2013 and her PhD degree in physics from the Université de Rennes (France) in 2016. In 2017, she continued her work on integrated micro-ring resonators based on polymers and porous silicon for sensor applications at the FOTON Institute (Lannion, France) as a postdoctoral fellow. She is currently working on polymer-based photonic sensor for environmental pollutants in a joint postdoctoral fellowship between the IMS Laboratory (Talence, France) and the Université de Sherbrooke (Canada). She conducts her research at the Université de Sherbrooke's Interdisciplinary Institute for Technological Innovation (3IT) and the CNRS International research laboratory - Laboratoire Nanotechnologies et Nanosystèmes (LN2)

L. Oyhenart obtained the Ph.D degree in electrical engineering from the Université de Bordeaux (France) in 2005. Currently, he is an Associate Professor at the Université de Bordeaux and develops his research activities in the IMS laboratory. His research interests include computational electromagnetics, photonic crystals, and energy harvesting.

T. Rouanet obtained his MSc in bio-nanotechnologies from the Université de Lille (France) in 2019. He is currently completing a PhD on the development and characterization of photonic structures for pollutant detection in co-supervision between the IMS laboratory (Talence, France) and the Université de Sherbrooke (Sherbrooke, Canada).

S. Joly is Associate Professor at the Université de Bordeaux in the IMS Laboratory (Talence, France), since 2013. He obtained his PhD degree in physics from the Université de Grenoble (France) in 2009. From 2010 to 2013, he undertook three postdoctoral positions, at the Institute of Molecular Science (Japan), at the IMEP-LAHC Laboratory (France), then at the CEA (France). He has been involved in nonlinear optics, laser, terahertz spectroscopy and infrared imaging research activities. His current research concerns evaluation of photonics components within the EDMINA Research Group at the Integration of Materials to Systems Laboratory (IMS, Bordeaux).

G. Beaudin obtained his PhD in electrical engineering at the Université de Sherbrooke (Canada) in 2015. In 2018, he completed a postdoctoral fellowship at the Université de Sherbrooke where his research activities concentrated on the realization of telecom photonic devices, as well as on photonic and plasmonic biosensors. He is now working as a research professional at the Université de Shebrooke on photonics and plasmonics, with new activities in quantum photonics. He conducts his research at the Université de Sherbrooke's Interdisciplinary Institute for Technological Innovation (3IT) and the CNRS International research laboratory - Laboratoire Nanotechnologies et Nanosystèmes (LN2).

M. Canva obtained his PhD degree in physics from the Université Paris-Sud in 1992. He then joined CNRS as full-time researcher in the Laboratoire Charles Fabry of the Institut d'Optique Graduate School (France). He was a visiting scholar at CREOL, University of Central Florida for two years (1996-1998) and for one year at Duke University (2009-2010). In 2014, he joined the CNRS International Research Laboratory LN2, where he currently serves as Director, at Université de Sherbrooke, where he is also an Associated Professor. His current interests focus on nano-bio-plasmonics and optical sensing instrumentation and systems for biomedical and environmental applications, especially including those based on plasmonics and, more generally, waveguide structures. He is co-author of over 100 publications in internationally peer-reviewed journals.

L. Bechou obtained his PhD degree in electronics from the University de Bordeaux (France) in 1998. Then, he joined the Integration of Materials to Systems Laboratory (IMS) at the Université de Bordeaux 1 as Associate Professor. Since 2010, he is a Full Professor in electronics and physics at the Université de Bordeaux. His research interests focus on "design for reliability" including the design, fabrication, characterization and aging effects of packaged optoelectronics and photonics devices based on the physics of light-matter interactions as well as the understanding of early degradation processes. Since 2010, he is head of the "Reliability Assessment of Micro and Nano-assembled Devices" research group (EDMINA) at IMS. He is the author or co-author of more than 180 regular papers and international conferences. He is an Associate Professor at the Université de Sherbrooke (Canada).

P.G. Charette obtained his PhD degree in biomedical engineering from McGill University (Canada) in 1994, followed by postdoctoral fellowships at the University of Auckland (New Zealand) and MIT (USA). He is a Full Professor of Electrical and Computer Engineering at the Université de Sherbrooke (Canada). He was a CNRS visiting scholar at the École Centrale de Lyon (France) in 2008-2009. His research interests include signal processing, numerical modeling, photonic biosensors, plasmonics, nanotechnology, and, quantum photonics. He has published over 50 journal papers and holds five patents.